Chapter 13
Simulation of Fluid Flow, Heat Transfer and Particle Transport Inside Open-Cell Foam Filters for Metal Melt Filtration

Eric Werzner, Miguel A. A. Mendes, Cornelius Demuth, Dimosthenis Trimis, and Subhashis Ray

13.1 Introduction

The removal of impurities from liquid metals inside ceramic foam filters (CFF) occurs predominantly through depth filtration, owing to the small size and concentration of inclusions. A deeper understanding of the relevant physical phenomena, involved in this process, is required in order to develop novel filters with improved characteristics. However, due to the high temperature and visual opacity of the melt, as well as due to the complex geometry of CFFs and the stochastic nature of the inclusion capture processes, it is extremely difficult, if not impossible, to obtain detailed information by means of conventional experimental techniques. In contrast to this, numerical simulations can naturally provide information on numerous physical quantities with high temporal and spatial resolution. Furthermore, they are less costly and time-consuming than laboratory trials, enabling comprehensive parametric studies that would be otherwise infeasible to conduct experimentally.

Depth filtration models can be broadly divided into two categories: (1) macroscopic or phenomenological models, which provide correlations or analytical expressions that describe the filtration phenomena in terms of empirical parameters, based

E. Werzner · C. Demuth · S. Ray (✉)
Institute of Thermal Engineering, Technische Universität Bergakademie Freiberg, Gustav-Zeuner-Str. 7, 09599 Freiberg, Germany
e-mail: ray@iwtt.tu-freiberg.de

M. A. A. Mendes
Instituto de Engenharia Mecânica, Instituto Superior Técnico, Universidade de Lisboa, Av. Rovisco Pais 1, 1049-001 Lisboa, Portugal

D. Trimis
Division of Combustion Technology, Engler-Bunte-Institute, Karlsruhe Institute of Technology, Engler-Bunte-Ring 1, 76131 Karlsruhe, Germany

C. G. Aneziris and H. Biermann (eds.), *Multifunctional Ceramic Filter Systems for Metal Melt Filtration*, Springer Series in Materials Science 337,
https://doi.org/10.1007/978-3-031-40930-1_13

on either experimental data or theoretical considerations and, (2) pore-scale models, which employ the solution of the governing equations for the melt flow and inclusion dynamics in two- or three-dimensional domains, considering either the true filter geometry or similar computer-generated structures. With the growing capacity and availability of high performance computers, the latter approach is becoming increasingly attractive. The results of pore-scale simulations also contribute to the development of improved macroscopic models, which are often sufficiently accurate for a quick assessment or the comparison of filter structures. An overview of the literature concerning the pore-scale modeling of metal melt filtration inside CFFs was given by Demuth et al. [1] and hence is not repeated here for brevity. This chapter addresses different more advanced issues arising in the detailed modeling of individual physical phenomena that occur during metal melt filtration and presents main results of several recent comprehensive parametric studies, which contributed to an improved understanding of the process and the design of better filter geometries. Further, it shows efficient methods for the determination of relevant effective properties, in particular, the effective thermal conductivity.

This chapter is structured as follows: In the subsequent part of this section, the basic mathematical formulation of the pore-scale model along with references dealing with its implementation are provided. This is followed by a discussion on the flow regimes and the particle capture mechanisms that are encountered during depth filtration inside CFFs. In Sect. 13.2, information on the generation of the geometric models as well as the characterization and scaling of filter geometries are provided. Methods for the determination of effective filter properties, in particular, the effective thermal conductivity, the hydraulic tortuosity, the viscous and inertial permeability coefficients as well as the filtration coefficient are discussed in Sect. 13.3. In the subsequent section, individual modeling issues are addressed. They include the propagation of the melt front during infiltration, the characteristics and modeling of turbulent flow, the agglomeration of inclusions and their accumulation during long-term operation. Section 13.5 presents the results of several numerical investigations dealing with the sensitivity of the filtration process with respect to process conditions and geometry parameters of the filter, followed by a conclusion from this research effort.

13.1.1 Modeling Strategy

In the following, the employed mathematical modeling is briefly outlined for the sake of completeness. For a detailed description of the pore-scale model and its implementation using the lattice-Boltzmann method (LBM), one may refer to Demuth et al. [1, 2] and Lehmann et al. [3].

The simulation of depth filtration inside open-cell foams at the pore-scale is typically carried out using an Euler–Lagrange approach. The flow of liquid metal is governed by the mass and momentum conservation equations for an incompressible, Newtonian fluid, known as:

$$\frac{\partial u_\mathrm{i}}{\partial x_\mathrm{i}} = 0 \tag{13.1}$$

$$\frac{\partial u_\mathrm{i}}{\partial t} + \frac{\partial}{\partial x_\mathrm{j}}\left(u_\mathrm{i} u_\mathrm{j}\right) = -\frac{1}{\rho_\mathrm{m}}\frac{\partial p}{\partial x_\mathrm{i}} + \frac{\partial}{\partial x_\mathrm{j}}\left[\nu\left(\frac{\partial u_\mathrm{i}}{\partial x_\mathrm{j}} + \frac{\partial u_\mathrm{j}}{\partial x_\mathrm{i}}\right)\right] \tag{13.2}$$

where u, ρ_m, ν and p denote the velocity, the density, the kinematic viscosity and the pressure of the melt, respectively. Additional terms may appear on the RHS of Eq. (13.2), e.g., for the residual stresses when using a turbulence model [2] or when buoyancy-induced convection due to the temperature-dependent density is considered [1]. In the latter case, the following energy conservation equation is also solved:

$$\rho c_\mathrm{p}\left[\frac{\partial T}{\partial t} + \frac{\partial}{\partial x_\mathrm{i}}(u_\mathrm{i} T)\right] = \frac{\partial}{\partial x_\mathrm{i}}\left(k\frac{\partial T}{\partial x_\mathrm{i}}\right) \tag{13.3}$$

Here, c_p, k and T stand for the specific heat capacity, the thermal conductivity and temperature, respectively. For simplicity, the inclusions are modeled as spherical particles, which are one-way coupled to the flow field. Their trajectories are determined by solving the equation of motion in a Lagrangian reference frame considering the most relevant forces:

$$\begin{aligned} m_p\frac{\mathrm{d}v_i}{\mathrm{d}t} = &\underbrace{(m_\mathrm{p} - m_\mathrm{m})g_i}_{\text{buoyancy}} + \underbrace{m_\mathrm{m}\frac{18\nu f s}{d_\mathrm{p}^2}(u_\mathrm{i} - v_\mathrm{i})}_{\text{drag}} \\ &+ \underbrace{m_\mathrm{m}\frac{Du_i}{Dt}}_{\text{pressure gradient}} + \underbrace{m_\mathrm{m}\left(\frac{Du_i}{Dt} - \frac{dv_i}{dt}\right)}_{\text{added mass}} \end{aligned} \tag{13.4}$$

where v denotes the velocity of the particles, g stands for the gravitational acceleration and f_S is a Stokes drag correction factor for higher particle Reynolds numbers. Further, $m_\mathrm{p} = \rho_\mathrm{p}\pi d_\mathrm{p}^3/6$ is the mass of a spherical particle with diameter d_p, which displaces a melt volume of mass $m_\mathrm{m} = m_\mathrm{p}\rho_\mathrm{m}/\rho_\mathrm{p}$. In the vicinity of the wall, the drag force increases, thereby reducing the probability for wall contact, which is not reflected by the drag term in Eq. (13.4). An approach to correct the obtained collision efficiency during the post-processing of the data was demonstrated by Heuzeroth et al. [4]. Once an inclusion comes in contact with the filter struts, its filtration probability depends on its ability to remain attached. In most numerical studies, a simple adhesion condition is adopted that assumes a particle remains attached once it gets in contact with the strut surface. This seems to be justified in view of the small kinetic energy of the inclusions, the strong capillary forces in metal melts and the possible sintering between the particle and the filter surface, particularly at the high temperatures during steel filtration. The same condition, however, should not be applied to water-model depth filtration experiments inside CFF, for which simulations conducted using the

same adhesion condition overpredicted the measured filtration efficiency by more than 53% [5].

The amount of data, generated during detailed pore-scale simulations also poses a challenge for the storage, visualization and analysis of the results. In order to address these issues, methods for the efficient compression and visualization of the large datasets were proposed by Lehmann et al. [6, 7].

13.1.2 Identification of Flow Regimes

In order to reliably characterize the flow regimes for open-cell foams, the Reynolds number according to Ruth and Ma is proposed [8], which is also termed as the Forchheimer number Fo and is defined as:

$$Fo = \frac{u_\mathrm{D} k_1}{\nu \mathrm{k}_2} \tag{13.5}$$

where u_D is the superficial average velocity in the direction of the main flow, which is related to the interstitial average velocity $\overline{u}$ and porosity ε according to $u_\mathrm{D} = \varepsilon \overline{u}$ and the ratio between viscous and inertial permeabilities, k_1/k_2, is chosen as the length scale. Methods for their determination are discussed in Sect. 13.3.3. Both coefficients appear in the Darcy-Forchheimer law, which describes the flow through porous media at a macroscopic level:

$$\frac{\mathrm{d}p}{\mathrm{d}x} = \underbrace{-\frac{\mu}{k_1} u_\mathrm{D}}_{\text{viscous losses}} \underbrace{- \frac{\rho_m}{k_2} u_D |u_D|}_{\text{inertial losses}} \tag{13.6}$$

It may be mentioned here that k_2 is also known as Forchheimer coefficient. Using Eq. (13.5) and reformulating Eq. (13.6), an expression for the inertial contribution to the total pressure drop, which consists of both viscous and inertial components, is obtained as:

$$\chi \approx \frac{Fo}{1 + Fo} \tag{13.7}$$

Figure 13.1 shows different regimes of flow through porous media as a function of Fo and the corresponding inertial contribution χ. For any flow with $Fo < 0.01$, the inertial contribution is $\chi < 1\%$, meaning that the flow can be considered to be purely viscous. Hence it can be described by the Stokes equation on the pore-scale and Darcy's law on the macro-scale. It is evident that the determination of k_1 using Darcy's law should always be carried out in this regime. For $0.01 < Fo < 1.0$, the flow can be termed inertial but it is still dominated by the viscous effects. Although recirculation zones form in the wake regions of the struts, they still remain stable due to the

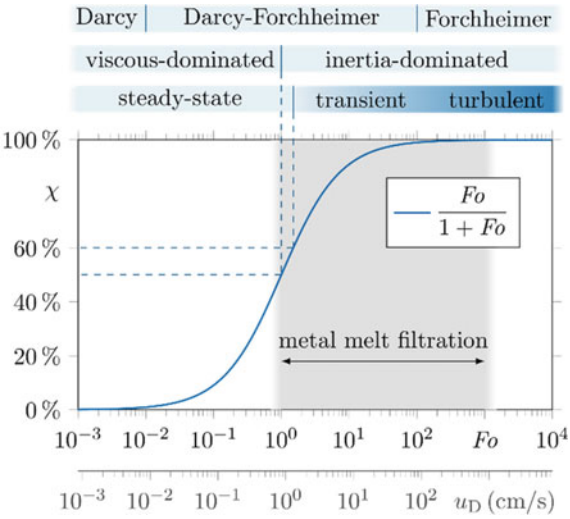

Fig. 13.1 Inertial contribution to total pressure drop χ and flow regimes for flow through porous media with respect to Fo. The second abscissa (gray) shows the corresponding superficial velocity u_D for two typical melt filtration systems: the filtration of (a) aluminum alloy AlSi7Mg inside a 30 ppi filter [9] and (b) AISI 4142 steel inside a 10 ppi filter [10]. Coincidentally, the ratio between u_D and Fo is nearly identical for these two systems

damping effect of viscosity, i.e., the flow can be considered as steady. The transition from steady-state to transient flow was observed to occur for different types of porous media at $\chi \approx 60\%$ [9], which corresponds to $Fo = 1.5$. Despite of its time-dependent nature, the flow still remains laminar in this regime, showing deterministic transients, similar to the vortices of a Kármán vortex street. It is important to note that numerical simulations in this regime require be initialized with a random perturbation of the velocity field in order to enforce the development of the transients, in particularly for regular geometries. As Fo increases further, the secondary flows turn out to be increasingly chaotic and for $Fo > 100$, i.e. $\chi > 99\%$, the flow can be considered fully inertial as well as turbulent.

As indicated in Fig. 13.1, industrial metal melt filtration processes cover a wide range of Fo, since their superficial velocities u_D vary from a few cm/s, e.g., for filtration during continuous casting, up to several m/s in case of gravity casting. While the former can sometimes be simulated as a steady-state problem on relatively coarse grids, the pore-scale simulation of the latter would require extremely high spatial and temporal resolution for capturing all scales of turbulence and the very thin boundary layers. Direct numerical simulations (DNS) of the flow in this regime are limited to small filter sections or periodic unit cells. For larger filter samples, turbulence closures and special wall treatments are required. For the sake of completeness, it may be mentioned that purely viscous flow occurs during centrifugal supergravity filtration using very fine CFFs of 100 pores per inch (ppi) and higher.

13.1.3 Capture Mechanisms

For the characterization of the inclusion behavior, it is important to distinguish between negatively buoyant particles, i.e., inclusions with higher density than the melt $\rho_p/\rho_m > 1$ and the positively buoyant ones, for which $\rho_p/\rho_m < 1$. While the former is typically the case for oxide inclusions in light metals, such as aluminum, the latter typically occurs for heavy metals, e.g., iron or steel melt. The main capture mechanisms of depth filtration and the definitions of the dimensionless numbers characterizing their magnitude are presented in Table 13.1. All dimensionless numbers scale with the particle diameter, either linearly for the case of direct interception or quadratically for inertial impaction and gravitational settling/buoyant rising. While large (negatively buoyant) inclusions are susceptible to all collision mechanisms, the small ones are almost exclusively captured by direct interception. In addition, for large positively buoyant inclusions, the force due to pressure gradient, exerted by the melt, can be significant. It acts towards the centre of curvature of the fluid pathlines [11], pushing inclusions away from the filter wall on the upstream side of the filter strut, thereby significantly reducing the particle capture on the front face. The conventional definition of the Stokes number, however, does not express this difference, discerning the filtration of larger oxide inclusions from light and heavy metals. Therefore, a modified Stokes number is suggested, which takes into account the density difference between the two phases. It is obtained from non-dimensionalization of the equation of motion, considering only the terms representing pressure gradient and Stokes drag, under the assumption of very small particle Reynolds number $Re_\mathrm{p} \ll 1$, for which the time derivative of the particle velocity $\mathrm{d}v/\mathrm{d}t$ approaches the substantial derivative of the fluid velocity $\mathrm{D}u/\mathrm{D}t$, and is presented in Table 13.1. As one can easily recognize, the sign of St_mod becomes negative for particles with density ratios $\rho_\mathrm{p}/\rho_\mathrm{m} < 1$, indicating the marked change in the particle dynamics. The pressure gradient term does not only affect the transport of particles in the wall-normal direction, but also the motion of larger particles inside vortices that occur at higher flow Reynolds numbers. While negatively buoyant particles are flung outward of the vortices due to their inertia, the positively buoyant particles or bubbles are pushed towards their core, resulting in a preferential concentration of inclusions in different regions depending on the density ratio. The resulting local increase in the particle concentration and the relative motion of nearby particles, which drift differently depending on their size, may facilitate the collision of smaller inclusions and the formation of larger agglomerates that are more likely to get captured due to the aforementioned mechanisms of depth filtration. In order to estimate the probability of preferential concentration due to this mechanism, the characteristic time scale of the macroscopic flow, $d_\mathrm{s}/\overline{u}$, in the definition of St_mod requires to be replaced by a time scale of the turbulent motion. It may be mentioned here that neutrally buoyant particles with $\rho_\mathrm{p}/\rho_\mathrm{m} = 1$, for which $St_\mathrm{mod} = 0$, closely follow the streamlines but can still experience a relative motion due to the curved flow field surrounding them.

Table 13.1 Dimensionless numbers characterizing the main mechanisms of particle capture during depth filtration of liquid metals

Collision mechanism	Dimensionless number	
Direct interception	Interception number	$d^* = \frac{d_\mathrm{p}}{d_\mathrm{s}}$
Inertial impaction/pressure gradient	Modified stokes number	$St_\mathrm{mod} = \frac{(\rho_\mathrm{p}-\rho_\mathrm{m})d_\mathrm{p}^2\overline{u}}{18\mu d_\mathrm{s}}$
Gravitational settling/buoyant rising	Gravitational number	$N_\mathrm{G} = \frac{\lvert\overrightarrow{g}\rvert d_\mathrm{p}^2(\rho_\mathrm{p}-\rho_\mathrm{m})}{18\mu\overline{u}}$

13.2 Modeling of Geometry

The numerical models of the filter geometries can be either artificially generated or reconstructed from 3D computed tomography (CT) scan images of real CFFs. Conventionally manufactured CFFs often exhibit a macroscopic gradient in their geometric properties, significant anisotropy and random local defects, either hampering the reproducibility of studies or demanding large representative volumes for numerical simulations. A costly repetition of experimental trials and subsequent averaging is necessary in order to obtain reliable results, as required e.g., for sensitivity analyses. Computer-generated random foams are a remedy to this problem, as they can be reproducibly manufactured using 3D printing techniques while capturing the essential geometric features of their real counterparts [4, 9]. They also allow variations of topological and morphological features, enabling comprehensive sensitivity analyses, and can be generated with periodic boundaries with arbitrary size, facilitating handling of the boundary conditions for the numerical simulations. Generation of the artificial random foams, employed in the studies presented later, was elaborately described by Abendroth et al. [12]. Besides random foams, the space-filling unit cells, such as cubic cell [13], Kelvin cell [14], or the Weaire-Phelan structure are also used as models for open cell foams. While in such cases, only a small physical domain needs to be simulated for obtaining the velocity field, the particle deposition can be predicted for a much larger porous medium, by considering an unfolded domain for the particle tracking, as has been shown by Werzner et al. [15]. Figure 13.2 shows different examples of numerical models for open-cell foams.

All structures are stored as volume meshes on a uniform Cartesian grid, consisting of either fluid or solid cubic elements (voxels). In order to improve the accuracy of the curved boundary representation and the computational efficiency of the particle–wall collision checking, the signed Euclidean distance field is employed. It is calculated with sub-voxel accuracy from the voxel mesh after smoothing using a Gaussian kernel.

Ceramic foam filters are self-similar within a certain ppi range, i.e., after appropriate normalization, not only their geometric characteristics, such as the average pore and strut diameter, the specific strut length and surface area, but also the permeability coefficients k_1 and k_2 do not significantly depend on pore count. This is evident

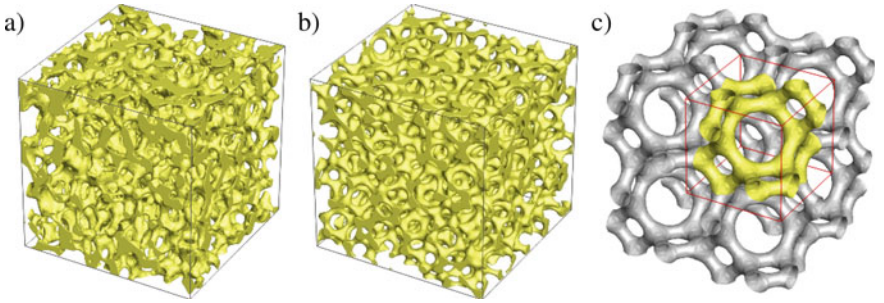

Fig. 13.2 Geometry examples: **a** CT scan reconstruction of a 30 ppi CFF with closed inner porosity and **b** computer-generated random foam with periodic boundaries, both comprising 216 pores, and **c** periodic section of 8 unit cells based on the tetrakaidekahedron (Kelvin cell) containing 16 pores

from Table 13.2, in which normalized geometric and hydraulic properties of 10, 20 and 30 ppi CFFs along with the computer-generated random foams are compared. The choice of an appropriate reference scale depends on the investigated problem. Here, and in previous studies [9, 13, 16], a length, calculated based on the volumetric pore density φ ($1/m^3$) was chosen, which is defined as follows:

$$L = \frac{1}{\sqrt[3]{\varphi}} \tag{13.8}$$

The inverse of L can be recognized as a more accurate pendant to the typical industrial ppi specification. The advantage of this reference length over other choices is its invariance with respect to morphological parameters, such as porosity or strut shape, and its clear definition. Values of φ and L are presented in Table 13.2.

13.3 Determination of Effective Properties Related to Metal Melt Filtration

Effective properties are required for the macroscopic modeling of the filtration process using the computationally efficient homogenization approach. They also serve to characterize filter geometries with respect to the different transport processes that occur during metal melt filtration.

13.3.1 Effective Thermal Conductivity

The effective thermal conductivity (ETC) is not only important for the characterization of the thermal shock resistance of filter foams but also required for simulations of

Table 13.2 Geometric and hydraulic characteristics of different CFFs and the computer-generated random foam [9, 13]

Filter material			Al_2O_3-C		Al_2O_3			Artificial foam
Nominal pore count		(ppi)	10	20	20	30	30	–
Geometry characteristics								
Pore density	φ	($1/m^3$)	$1.03 \cdot 10^7$	$3.54 \cdot 10^7$	$1.13 \cdot 10^7$	$3.95 \cdot 10^7$	$4.03 \cdot 10^7$	–
Reference length	L	(mm)	4.60	3.05	4.45	2.94	2.92	–
Porosity		(%)	80%	78%	78%	79%	81%	80%
Spec. surface area	S	(m^2/m^3)	593	899	655	949	964	–
Spec. projected area	S_P	(m^2/m^3)	147	248	153	246	242	–
Strut diameter	d_{strut}	(mm)	0.91	0.75	0.86	0.55	0.55	–
Window diameter	d_{win}	(mm)	3.80	2.84	3.55	2.32	2.29	–
Pore diameter	d_{pore}	(mm)	6.05	3.81	6.21	3.85	3.82	–
Normalized geometry parameters								
Surface area	$S \cdot L$		2.73	2.74	2.92	2.79	2.81	2.55
Projected area	$S_P \cdot L$		0.68	0.76	0.68	0.72	0.71	0.65
Strut diameter	d_{strut}/L		0.20	0.25	0.19	0.19	0.19	0.22
Window diameter	d_{win}/L		0.83	0.93	0.80	0.79	0.79	–
Pore diameter	d_{pore}/L		1.32	1.25	1.39	1.31	1.31	1.25

(continued)

Table 13.2 (continued)

Filter material			Al_2O_3-C		Al_2O_3			Artificial foam
Hydraulic properties								
Tortuosity	τ		1.15	1.14	1.13	1.15	1.14	1.11
Viscous permeability	k_1/L^2		$8.23 \cdot 10^{-3}$	$8.08 \cdot 10^{-3}$	$7.98 \cdot 10^{-3}$	$7.62 \cdot 10^{-3}$	$7.93 \cdot 10^{-3}$	$9.15 \cdot 10^{-3}$
Inertial permeability	k_2/L		$4.82 \cdot 10^{-1}$	$4.48 \cdot 10^{-1}$	$6.03 \cdot 10^{-1}$	$4.95 \cdot 10^{-1}$	$4.88 \cdot 10^{-1}$	$7.14 \cdot 10^{-1}$

energy transport using the homogenization approach. Mendes et al. [17]. proposed a simple and effective method for its determination that relies upon the predicted ETC under vacuum condition $k_{\mathrm{eff,s}}$, which is determined for $k_\mathrm{f}/k_\mathrm{s} = 0$, where the subscripts "f" and "s" stand for the fluid and the solid phases, respectively. The numerical evaluation of $k_{\mathrm{eff,s}}$ requires considerably less computation time compared to solving for the complete porous medium since the calculation in the fluid domain, which constitutes the largest volume fraction equal to the porosity, can be avoided. In order to arrive at the final recommendation, detailed numerical investigations were carried out by considering two artificial and four real open-cell foams. They demonstrated that $k_{\mathrm{eff,s}}$ contains all necessary structural information as far as the ETC is concerned. Therefore, the ETC of the porous medium for any k_f can be evaluated from a simplified model, which was proposed as:

$$\tilde{k}_\mathrm{eff} = b\tilde{k}_\mathrm{min} + (1-b)\tilde{k}_\mathrm{max} \tag{13.9}$$

where $\tilde{k} = k/k_\mathrm{s}$ is the dimensionless thermal conductivity, normalized with respect to k_s, while $\tilde{k}_\mathrm{min}$ and $\tilde{k}_\mathrm{max}$ are the minimum and the maximum bounds of the dimensionless ETC, respectively. The only adjustable parameter b in Eq. (13.9) can be evaluated from $k_{\mathrm{eff,s}}$ as follows:

$$b = \frac{\tilde{k}_{\mathrm{max,s}} - k_{\mathrm{eff,s}}}{\tilde{k}_{\mathrm{max,s}} - \tilde{k}_{\mathrm{min,s}}} \tag{13.10}$$

where the additional subscript "s" stands for the corresponding values of thermal conductivities, evaluated at vacuum condition, i.e., for $k_\mathrm{f}/k_\mathrm{s} = 0$. Mendes et al. [17] also demonstrated that the use of lower and upper Hashin-Strikman bounds [18] for $\tilde{k}_\mathrm{min}$ and $\tilde{k}_\mathrm{max}$, respectively, performs the best for most of the investigated cases. Since Eq. (13.9) is valid for any $\tilde{k}_\mathrm{f} = k_\mathrm{f}/k_\mathrm{s}$, the proposed model can also be used for the indirect evaluation of ETC in presence of hazardous fluids, like liquid metals. An experimental verification of the proposed model was presented by Wulf et al. [19]. They measured the ETC of open-cell FeCrAl alloy metal foams with different porosities and pore dimensions using the transient plane source (TPS) method at room temperature and observed reasonably good agreements with the predictions obtained from the model of Mendes et al. [17].

In principle, $k_{\mathrm{eff,s}}$, required for the determination of b, could also be measured. However, since it is extremely difficult to conduct experiments under true vacuum condition, Mendes et al. [20] proposed to measure the ETC in presence of a commonly available fluid, like air or water, and evaluate the parameter b from an equation similar to Eq. (13.10), indicated by replacing the second suffix "s" by "ref" which stands for the reference fluid instead of the vacuum condition. Their results show that a lower thermal conductivity working fluid, like air, is the most suitable for all investigated cases, although water may also be used if the thermal conductivity of the solid matrix is also sufficiently high.

Subsequently, an extension of this model was also proposed by Mendes et al. [21] consisting of two adjustable parameters those can be determined from the detailed numerical predictions of $k_{\text{eff,s}}$ and $k_{\text{eff,ref}}$, where the latter is evaluated in the presence of a reference fluid with known $\tilde{k}_{\text{f}}$. The model is quite similar to that in Eq. (13.9) except for the fact that $\tilde{k}_{\text{min}}$ is replaced by $\tilde{k}_{\text{a}}$, which is given as:

$$\tilde{k}_{\text{a}} = \left[\frac{a}{\tilde{k}_{\text{min}}} + \frac{1-a}{\tilde{k}_{\text{max}}} \right]^{-1} \tag{13.11}$$

where a is the second adjustable parameter. However, instead of using the lower and the upper Hashin-Strikman bounds [18] the use of equivalent thermal conductivities for the serial and the parallel arrangements of solid and fluid phases were recommended for $\tilde{k}_{\text{min}}$ and $\tilde{k}_{\text{max}}$, respectively. Using these values, the model parameters b and a can be sequentially determined from $k_{\text{eff,s}}$ and $k_{\text{eff,ref}}$, respectively. Quite clearly, the original model of Mendes et al. [17] can be easily retrieved by setting $a = 1$ for which, $\tilde{k}_{\text{a}} = \tilde{k}_{\text{min}}$ is obtained from Eq. (13.11). Performance of the model was investigated by comparing its estimation with the results obtained from the detailed numerical simulations and the predictions obtained from the original model. It was clearly demonstrated that the modified model performs extremely well for all investigated structures, provided the reference fluid is appropriately chosen.

In order to account for the thermal radiation, which is expected inside porous medium in the presence of metal melt at high temperature, Talukdar et al. [22] proposed a 3D numerical model that solves combined conduction–radiation heat transfer employing the finite volume method (FVM), combined with the blocked-off region approach, that is capable of handling the grey–diffusive behavior of the strut surfaces. The model, which is represented by the overall energy balance equation and accounts for the radiative heat flux from the solution of the 3D radiative transfer equation (RTE), uses the voxel based information of the porous medium for representing the geometry that is employed also for solving other conservation equations and hence eliminates the complexity of grid generation. The representative porous media, considered for this investigation, are the cubic cell and the honeycomb structures. The effective thermal conductivities evaluated using the model for different temperatures, emissivities and thermal conductivities of the solid and different absorption coefficients of the fluid were compared with that obtained from FLUENT 6.3 as well as the data available in the literature and good agreements were observed.

After establishing the detailed conduction–radiation model [22], Mendes et al. [23] applied it for evaluating the ETCs of three real foams with different porosities and pore counts. Other than this model [22], Mendes et al. [23] also considered yet another detailed but decoupled model, where pure conduction and pure radiation are separately solved while disregarding the contribution of the other mode of heat transfer, and proposed three simplified one-dimensional (1D) models, based on homogenization approach. The simplified models require information about the ETC due to pure heat conduction $k_{\text{eff,C}}$, calculated from the detailed 3D simulation [17,

20, 21], and the extinction coefficient β, estimated from the 3D CT-scan data using the image processing technique by the projection method [24]. The ETCs predicted by these four models were compared with the data obtained by employing the most accurate detailed model of Talukdar et al. [22], those were considered as reference values in order to determine the accuracy of other simplified models. It was observed that all simplified models perform reasonably well, provided the maximum value of the extension coefficient is chosen, while the alternative detailed and decoupled model consistently underpredicts the ETC for all cases.

An experimental validation of two simplified 1D homogeneous models, proposed by Mendes et al. [23], was presented by Mendes et al. [25], who measured the ETC of two FeCrAl alloy foams with similar porosity but considerably different pore dimensions at temperatures ranging from 130 to 850°C using the panel test technique. The first model (Model-1) of Mendes et al. [25] solves the coupled conduction–radiation heat transfer using the 1D RTE, while their second model (Model-2) employs the extremely simplified Rosseland approximation in order to account for the thermal radiation. As mentioned earlier in the last paragraph, both 1D homogeneous models, however, require $k_{\text{eff,C}}$ and β as inputs. Comparison of the results shows that both simplified models are efficient alternatives to the detailed model for the determination of ETC at high temperatures. Although Model-2 is extremely simple, it may still be used provided the optical thickness of the porous medium is reasonably high. For more accurate predictions, however, Model-1 was recommended by Mendes et al. [25], irrespective of the value of β.

Owing to the manufacturing process, porous foams often exhibit a certain amount of anisotropy and also contain microscopic porosities that cannot be captured by 3D CT-scan images with the available resolution. Although the total porosity ε_{T} of the foams can be accurately determined by measuring their weights, dimensions and the density of the strut material, the microscopic porosity ε_{m}, which is extremely sensitive to the manufacturing process and may vary between 5 to 25%, can only be roughly estimated. The macroscopic porosity ε_{M}, on the other hand, can be evaluated from the measured ε_{T} and the estimated ε_{m} as follows:

$$\varepsilon_{\text{M}} = \frac{\varepsilon_{\text{T}} - \varepsilon_{\text{m}}}{1 - \varepsilon_{\text{m}}} \tag{13.12}$$

Increase in the microscopic porosity has two opposing effects as far as the ETCs of porous foams are concerned: (1) it reduces ε_{M} according to Eq. (13.12) since ε_{T} remains constant and hence increases the solid fraction or the effective strut volume (that also contains microscopic pores) available for heat conduction and (2) it reduces the thermal conductivity of the modeled struts or the solid fraction, which could be estimated from the upper Hashin-Strikman bound [18]. Considering these issues, Mendes et al. [26] investigated the effects of anisotropy and microscopic porosity on the ETC of 10 and 45 ppi porous foams using both detailed numerical simulations and the simplified model of Mendes et al. [17]. They observed that for the considered foam samples, ETC increases with the increase in ε_{m}, which, however, may not be the case for other foams owing to the opposing effects of ε_{m} as mentioned earlier.

Nevertheless, they concluded that the proposed simplified model of Mendes et al. [17] performs extremely well with significantly reduced computational effort and hence may be employed for investigating the sensitivity of ETC on different structural parameters.

The simplifications for modeling the ETC of porous foams, proposed by Mendes et al. [17, 25] in the presence of both conduction and radiation were validated later by Mendes et al. [27]. They measured the ETC of two anisotropic 10 ppi pure alumina large foam samples with almost similar porosity $\varepsilon_T \approx 0.89$ and other geometric parameters using the TPS technique for average foam temperatures T_{av} ranging from 22 to 750°C. The average ETCs of two samples were compared with the predictions obtained using Model-1 of Mendes et al. [25]. The predicted results exhibited the expected effects of anisotropy and estimated microscopic porosity on the directional ETC, as shown in Fig. 13.3. The measured ETC in a particular direction and the predicted ETC in the same direction, obtained after the proposed directionally weighted averaging, compared extremely well for the complete range of investigated temperature. Based on this observation, they concluded that the ETC, measured employing the TPS technique, are to be considered as the directionally averaged value of the ETCs in three mutually perpendicular directions. The investigation also clearly demonstrated the potential of the simplified modeling approach for characterizing even the directional ETC of open-cell foams, based on their structural information that could be obtained solely from the 3D CT-scan data.

Using the modeling tools developed by Mendes et al. [17] and Talukdar et al. [22], the variations in the ETC of a tetrakaidecahedra unit cell as functions of ε, k_s and T_{av} due to combined conduction and radiation were examined by Patel et al. [14]. In addition, they also investigated the effects of surface reflectivity, pore density and porosity on the radiative properties of the structures, for which a pure radiation heat

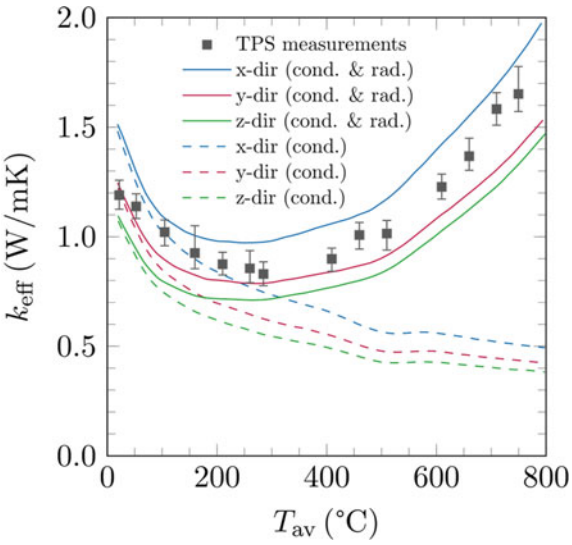

Fig. 13.3 Directional dependence of predicted ETC and experimental data (lines indicate the model predictions) [27]

transfer solver was developed and employed. In order to develop useful correlations, three different ETCs were predicted: (1) due to pure heat conduction i.e., without radiation $k_{\text{eff,C}}$ [17], (2) due to pure radiation heat transfer i.e., without conduction $k_{\text{eff,R}}$ [14] and finally (3) due to combined conduction and radiation k_{eff} [22], which is considered as the reference value for comparison. From the acquired data, three different correlations were proposed with varying degree of complexities. The final correlation, obtained by superposing $k_{\text{eff,R}}$ and $k_{\text{eff,C}}$ with an adjustable coefficient that takes into account the coupling between radiation and conduction heat transfer, was recommended.

13.3.2 Hydraulic Tortuosity

The probability of contacts between the inclusions and the filter web strongly depends on the tortuosity of the flow pathlines. It can be directly evaluated from the velocity field obtained from pore-scale simulations as follows [28]:

$$\tau = \frac{\langle |u| \rangle}{\langle u_x \rangle} \tag{13.13}$$

Here, the angle brackets $\langle \cdot \rangle$ denote spatial averages, $|u|$ is the velocity magnitude and the direction x stands for the direction of the bulk flow. The hydraulic tortuosity was evaluated for the Stokes flow regime, i.e. at $Fo \ll 1$ and hence it is considered as one of the characteristics of the porous media. Values for different open-cell foams are presented in Table 13.2.

13.3.3 Viscous and Inertial Permeability

The permeability coefficients, appearing in Eq. (13.6), are required for the design of filtration systems, the identification of the flow regime and the simulation of flow through porous media using the homogenization approach. While k_1 can be evaluated in a straightforward manner employing Darcy's law from a single pore-scale simulation in the Stokes regime, the numerical determination of k_2 from a single simulation in the purely inertial regime is computationally challenging for real filter geometries. However, once k_1 is known, an estimate can be obtained by solving the Darcy-Forchheimer law for k_2 using data from a simulation at $Fo \approx 1$, where the inertial contribution to the total pressure drop is already significant but the flow still remains steady. Since the estimation of Fo and hence setting up of such a simulation itself requires the prior knowledge of k_2, its guess value needs to be provided. On the basis of a momentum balance, one can arrive at an extremely simple expression for k_2 of porous media in the limit of high porosity, which reads as [2]:

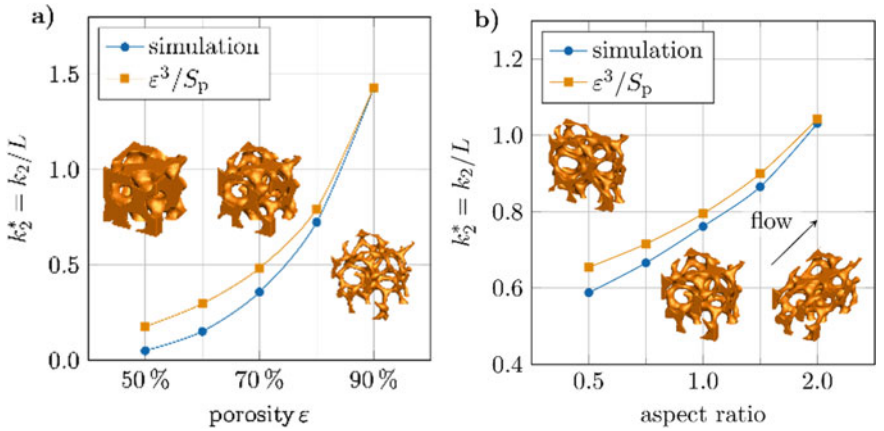

Fig. 13.4 Predictions of dimensionless inertial permeability coefficient k_2^* obtained from detailed pore-scale simulations and the correlation of Eq. (13.14) for artificial open-cell foam structures with **a** different porosity and **b** different aspect ratio at 85% porosity. The simulated foam samples comprises 216 pores

$$k_2 = \frac{\varepsilon}{S_p} \tag{13.14}$$

where S_p is the cumulative specific surface area, projected in the direction of the main flow, which can be easily estimated from a voxel representation that can be obtained from 3D μCT scan images. Since S_p contains direction-dependent information, it is able to handle the anisotropy, which is present in most CFFs with lower pore count [9]. A comparison of Eq. (13.14) with the predictions obtained from detailed pore-scale simulations for artificial random foams with different porosity and aspect ratio is presented in Fig. 13.4. Accurate correlations for k_1 and k_2, which also account for the effect of tortuosity, were developed by Jorge et al. [13]. Values of k_1 and k_2 for CFFs with pore counts of 10, 20 and 30 ppi are presented in Table 13.2. A model for the prediction of the mechanical behavior of CFFs during filtration employing k_1 and k_2 was proposed by Lange et al. [16].

13.3.4 Filtration Coefficient

Assuming depth filtration to be the dominant mode of particle retention and a homogenous porous medium, the variation in the particle concentration c inside the melt, is governed by:

$$\frac{\mathrm{d}c}{\mathrm{d}x} = -\lambda c \tag{13.15}$$

where λ is the filtration coefficient. Solving Eq. (13.15) yields the depth filtration law:

$$\eta(x) = 1 - \mathrm{e}^{-\lambda x} \tag{13.16}$$

Here, $\eta(x)$ is defined as the fraction of inclusions with respect to the total amount of suspended inclusions, captured by the filter up to a certain depth x, and is straightforward to obtain from the pore-scale simulation of the filtration process. A simplified deposition model for simulations using the homogenization approach, which also takes into account the variation in λ with the flow velocity was proposed by Asad et al. [10].

In the limit of very high porosity, λ can also be estimated from simple geometric considerations since the filter can then be approximated as a skeleton of thin wires that do not significantly affect the flow field and intercept all inclusions within a distance of $d_\mathrm{P}/2$. Assuming that approximately $2/3$ of the available cumulative strut length contributes to the filtration, neglecting the overlapping of the struts in flow direction and introducing the specific strut length l^+, the following simple expression for the filtration coefficient could be obtained:

$$\lambda_\mathrm{lim} = \frac{2}{3} d_\mathrm{P} l^+ \tag{13.17}$$

13.4 Selected Modeling Issues

In the following, the modeling of different physical phenomena involved in the depth filtration process will be discussed, which have received considerably less attention in the existing literature on metal melt filtration.

13.4.1 Geometry Change During Long-Term Operation

During long-term operation of CFFs, e.g., in the course of continuous casting, or while filtering highly contaminated melts, the accumulation of inclusions, deposited inside the filter is expected to alter its effective geometry. In order to investigate how the change in filter geometry affects the melt flow and the capture of inclusions, a model was developed for the filtration of aluminum during continuous casting inside a 30 ppi CFF [29]. The deposited inclusions are modeled as an impermeable rigid porous sediment, whose porosity was treated as a free parameter with $\varepsilon_\mathrm{sed} = 40, 60$ and 80%. For every fluid voxel containing filtered particles, the effective volume of the sediment is calculated. Whenever it exceeds the voxel volume, its state is changed from fluid to solid, resulting in a stepwise relocation of the filter surface. As the real loading process is extremely slow compared to the temporal

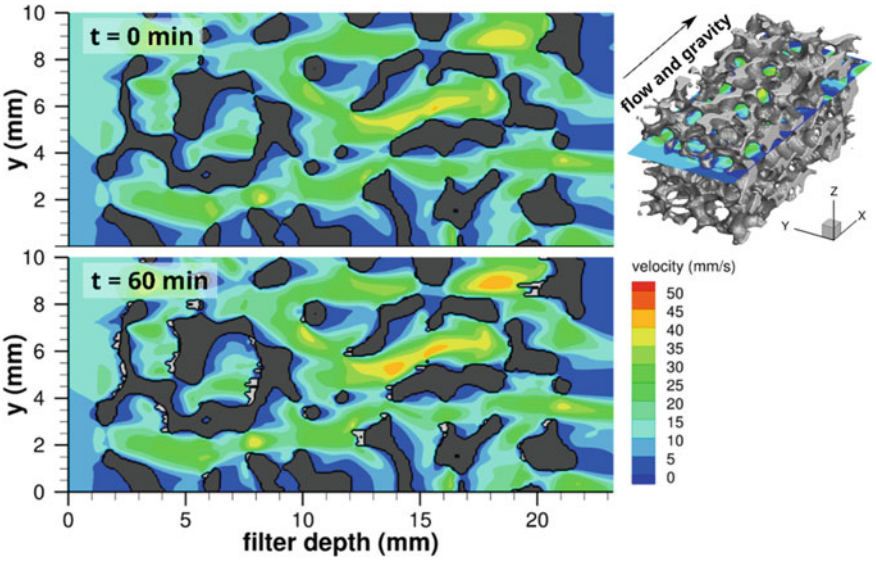

Fig. 13.5 Modification of filter geometry and distribution of velocity magnitude during long-term filtration for a sediment porosity of $\varepsilon_{sed} = 60\%$. A number of 10^7 Al_2O_3 particles with 20 µm diameter were inserted randomly on a plane upstream of the filter. The liquid aluminum was driven with a superficial velocity of 10 mm/s. The filter geometry was reconstructed from a CT scan of a 30 ppi Al_2O_3 foam, obtained with a resolution of 65 µm, which was used also for the LBM simulation. The computational domain was extended by one filter length in the upstream and downstream directions

resolution required for the particle tracking, its simulation would cause prohibitively high computational costs. Therefore, the process was accelerated by imposing a 21-fold increased concentration of impurities. This adjustment is possible as the flow is quasi-steady and since particle-particle interactions are negligible at the low volume fraction of particles inside the melt of 10^{-5} (10 ppm), assumed for the investigated process. In this manner, a physical duration of 60 min could be captured by simulating only 9 average residence times of the melt inside the filter.

Figure 13.5 shows the modification of the filter geometry and the associated change in the velocity distribution assuming a sediment porosity of 60%. As visible from the figure, after 60 min, the filtered particles have formed sediments on the upstream faces of the filter struts, that protrude into the pores and cause a marginal but recognizable increase in local melt velocity. The time-variations of different filter characteristics are presented in Fig. 13.6. The filter loading, which is the fraction of the initially available pore volume occupied by the sediments, remains relatively low within the observed time. Nevertheless, the modification of the filter geometry results in a significant increase in filtration efficiency and also pressure gradient $p\prime$. Depending on sediment porosity, the filtration coefficient λ, which is estimated from the instantaneous filtration efficiency assuming the validity of the depth filtration law, increases between 18% and 76%. While this variation occurs linearly over time

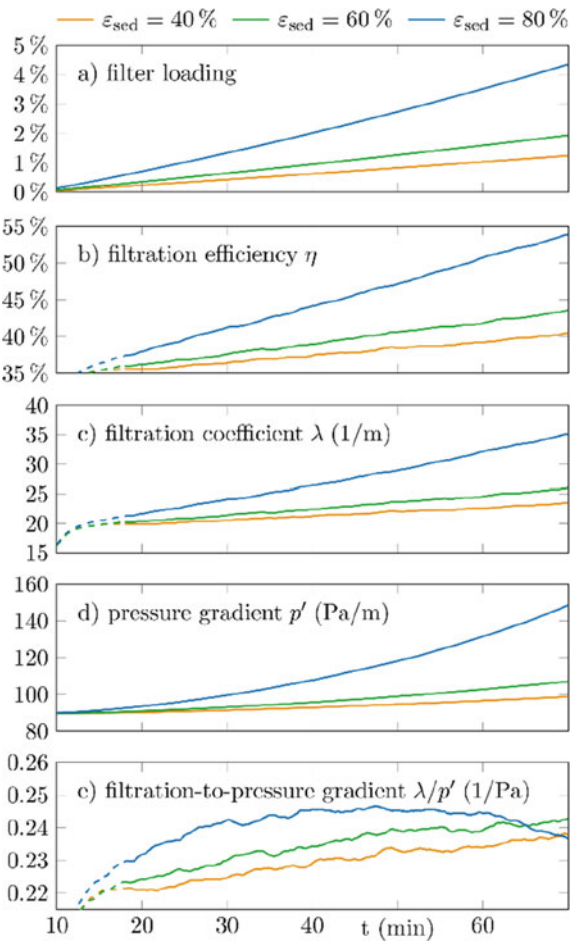

Fig. 13.6 Time-variations of filter loading and different filtration-related characteristics during long-term filter operation assuming different porosities of the deposited sediments ε_{sed}. In the initial stage, the filtration efficiency and related quantities cannot be accurately evaluated as the filter is not yet completely filled with contaminated melt (indicated by dashed lines). Due to the artificial acceleration of the loading process, this phase appears extended in physical time

($\overline{R^2} = 1.00$), the pressure gradient tends to increase quadratically ($\overline{R^2} = 0.97$). Hence, in the initial stage, when the change in pressure gradient is small, the filter efficiency in terms of the ratio $\lambda/p\prime$ increases with time. For $\varepsilon_{sed} = 80\%$ it attains a maximum after 37 min, when the filter is loaded by 2.5%. This optimal filter loading is also expected for the cases with lower sediment porosity, but could not be observed within the simulated time duration.

13.4.2 Agglomeration

The intentional agglomeration of small inclusions to form larger aggregates, that are more likely to be captured by the filter, may benefit their filtration. Particles can

only collide when they experience a relative motion with respect to each other, either due to velocity shear, e.g., in boundary layers and vortices, or due to the difference in their slip velocity that results from a difference in properties, particularly size and density. Furthermore, they must overcome the viscous force [4], which is a result of the squeezed film flow in the gap between two particles. Once collided, the inclusions are expected to adhere to each other, as this state is favorable in terms of surface energy. Furthermore, at higher temperature, sintering takes places that creates a strong bond between the particles. It is obvious that the probability for agglomeration strongly depends also on the particle concentration, which determines the average distance between the particles. Although it is low for most melt filtration systems, i.e., in the order of ppm, the effect of preferential concentration in highly turbulent flows may increase the local concentration to a level, where collisions are more probable to occur. Since an ideal structure for the promotion of agglomeration has to meet different requirements than a filter, composite structures, consisting of several functional layers, have to be considered.

In order to investigate the potential of agglomeration, leading to the improved filtration of smaller inclusions, the filtration of liquid steel was simulated using an agglomeration model. A variety of composite filter structures, consisting of layers of Kelvin cells with 85% porosity, measuring either 5 or 10 mm cell width, as depicted in Fig. 13.7a were tested. The flow of liquid steel (AISI4142) entering with a velocity of $u_{\mathrm{D}} = 10\mathrm{cm/s}$ was simulated, resulting in $Fo = 10.5$ and 21.0 with corresponding $Re_{\mathrm{strut}} = 160.5$ and 321.0 for the small and large cells, respectively. The simulations were carried out with periodic boundary conditions in the spanwise direction. A number of 10^7 SiO_2 particles were randomly inserted at a rate, which corresponded to an average volumetric concentration of 200 ppm. The collision radius of the agglomerates was calculated according to the closely-packed sphere model, considering an agglomerate porosity of 50%. In order to reduce the computational time for collision checking, the linked-cell method was employed.

As shown in Fig. 13.7b, approximately only 6% of the inclusions form agglomerates. The highest formation of agglomerates is observed for a structure with fine pores, followed by a single layer of large pores (marked in red). Irrespective of the spatial distribution, the amount of agglomeration tends to grow with the fraction of small pores. It was further observed that agglomeration tends to decrease with filter depth, as the number of potential collision partners in the vicinity of an inclusion or agglomerate becomes smaller due to previous agglomeration events and filtration. The vast majority of agglomerates consisted of only two inclusions whereas the largest one comprised 8 inclusions and measured 25 μm, which is still relatively small. Although the agglomerates are more likely to get trapped by a filter strut, particularly due to increased probability of direct interception, their contribution to the overall filtration efficiency (in terms of filtered particle volume) is still lower than their volume fraction among all particles, since they spend less time inside the filter than solitary inclusions. A comparison of the filtration efficiencies, shown in Fig. 13.7a, with those obtained from simulations carried out without the agglomeration model showed an average improvement of only 1%. Hence, agglomeration has a negligible effect on overall filtration, at least for the conditions considered here. The

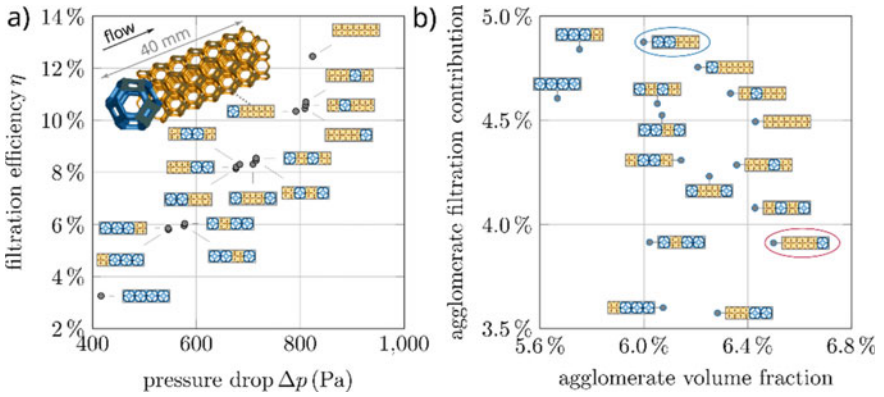

Fig. 13.7 Filtration of SiO_2 inclusions of 10 μm diameter from liquid steel (AISI4142) through composite filters consisting of differently sized Kelvin cells, taking into account the effect of agglomeration: **a** filtration efficiency and pressure drop, **b** contribution of agglomerates to total filtration versus the agglomerate formation, defined as fraction of agglomerates with respect to the total volume of impurities

safe removal of larger agglomerates is crucial, since they are more detrimental to the quality of the cast part than small inclusions. As visible from Fig. 13.7b, composite structures, consisting of a coarse layer followed by a fine one, are performing better in this respect (marked in blue). However, an assessment of the usefulness of composite structures with functionalized zones for intentional agglomeration of smaller inclusions would require further studies. The investigations should also include higher bulk flow velocities in order to study the effect of turbulence as well as particle size distributions and particles with different densities or bubbles.

13.4.3 Infiltration Process

In all numerical studies on liquid metal filtration, known to the authors, the initial stage of the process, during which the melt penetrates into the filter, also termed as priming, is neglected and the structure is initialized as being completely filled with the molten metal. However, this initial phase could be particularly critical as the melt may freeze and hence block the pores or the filter may get damaged due to the thermal shock. Further, Marangoni convection is expected to significantly influence the melt propagation into the porous medium. An additional infiltration resistance follows also from the capillary pressure and the change in momentum, as the flow gets deflected by the struts of the filter. The necessity of reliable priming and the desired high filtration efficiency may pose conflicting requirements on the filter design, e.g., as far as the pore density is concerned. Therefore, the computer-aided development of improved filter geometries should also include the simulation of the initial stage.

For modeling of the infiltration process in the LBM context, a free-surface model was adopted [30]. In this model, the mass and momentum conservation equations are solved only for the fluid phase. The gas–liquid interface is captured using the volume-of-fluid approach and capillary effects are considered by the continuum surface force model. The present implementation handles the wetting behavior using a fictitious extension of the gas-liquid interface into the solid with a prescribed contact angle. While the code was successfully validated for canonical problems, numerical instabilities occurred during simulations of the real infiltration process. The imposition of high Laplace pressure, which follows from the high surface tension coefficient σ of the melt and the small radii of curvature inside the small pores of the CFF, causes a strong distortion of the mesoscopic particle distribution, used by the LBM for representing the fluid state. Furthermore, parasitic currents were observed near the contact line. The identified instabilities could only be avoided by increasing the spatial resolution to a level, at which the strut diameter was resolved with a number of voxels, corresponding to $1.6 \times 10^{-4} Re_{\mathrm{Pore}}/Ca$, where Re_{Pore} is the Reynolds number based on the pore diameter and the capillary number is defined as $Ca = \mu\overline{u}/\sigma$. Since the resulting grid resolution would be prohibitively high for practical simulations of the metal melt filtration, the applicability of the free-surface LBM in this context is limited, unless an adaptive grid refinement of the interface is implemented. Another difficulty arises from the fact that in the LBM, the time step size is indirectly defined through the choice of the sound speed, which serves as a numerical parameter that can be adjusted within certain limits. While the sound speed is often artificially reduced to accelerate the time marching, this practice introduces problems when gravitational acceleration is included, since the large hydrostatic pressure of the liquid metal then introduces a significant density variation along the height, which violates the assumption of weak compressibility, required by the LBM.

Nevertheless, in order to demonstrate the capability of the model and to investigate the effect of the filter coating, the infiltration of aluminum into a CFF was simulated in 2D for different wetting angles at a reduced surface tension, where the metal is fed from the bottom. The results, presented in Fig. 13.8, show that even at reduced σ, the flow behavior is strongly determined by the capillary action. Once the melt touches the solid strut surface, capillary waves are generated at the interface, which oscillate much faster than the average interstitial velocity. At the smaller windows, particularly for the simulation with higher wetting angle, the melt stagnates, causing a redistribution of the melt flow. Once the Laplace pressure is overcome, the melt discharges into the adjacent pore, during which velocities of more than 20 times the inlet velocity as well as large vortices are observed. This discontinuous filling of the pores is also visible from surges in the average pressure, measured on the inlet plane, that are also more pronounced for higher wetting angle.

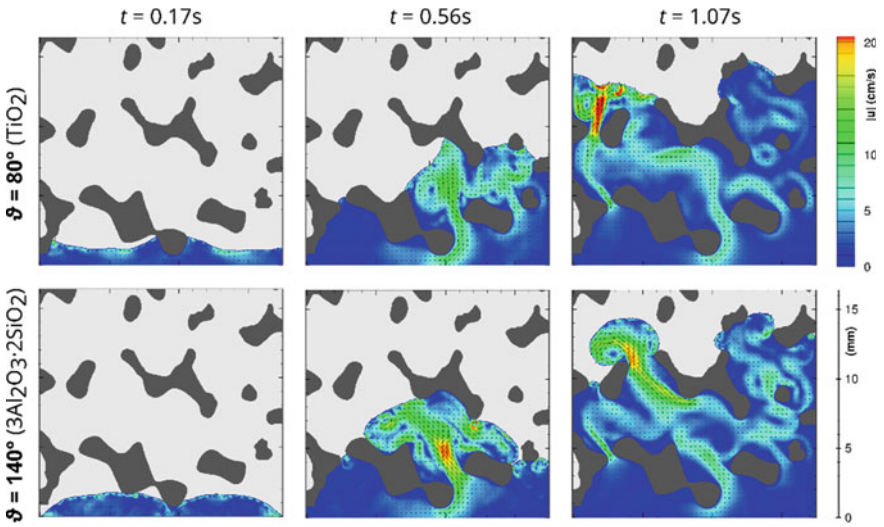

Fig. 13.8 Distribution of the velocity magnitude in the liquid phase during infiltration of Al_2O_3 CFF with a superficial velocity of $u_D = 1$cm/s at different wetting angles ϑ, measured by Voigt et al. [31] ($Re_{Pore} = 117$, $Ca = 1, 17 \times 10^{-4}$, $Bo = 6, 72$ and direction of gravity $\downarrow$)

13.4.4 Non-isothermal Modeling

Although heat transfer plays a crucial role for the filtration process due to the expected temperature gradients in the melt and the sensitivity of the melt properties, particularly density, viscosity and surface tension, with respect to temperature, its variation is often neglected in numerical simulations and hence the energy conservation equation is not invoked. Demuth et al. [1] developed a model, which couples the LBM for the prediction of the fluid flow with a finite volume method (FVM) for solving the energy equation, considering the temperature-dependent melt density and viscosity. The viability of the model was demonstrated by simulating the filtration of aluminum for conditions as present during continuous casting. They reported the development of buoyancy-induced secondary flows, which led to higher heat losses and a delayed entry of the inclusions. For the considered boundary conditions, however, the effect of temperature-dependent viscosity on the flow field was found to be negligible.

13.4.5 Characterization and Modeling of Turbulence

Selection of a suitable modeling approach for turbulence inside open-cell foams requires a good understanding of its nature. In order to characterize turbulence inside CFFs, a direct numerical simulation (DNS) of flow through an idealized open-cell

foam consisting of Kelvin cells was carried out at $Fo = 64$ ($\chi = 98\%$). The simulated unit cell was scaled to dimensions of $5 \times 5 \times 5$mm, as depicted in Fig. 13.9a, and was discretized using a voxel mesh with 4.9 µm resolution, allowing to capture flow details with very fine scales. The corresponding pore density of $\varphi = 1.6 \times 10^7 1/\mathrm{m}^3$ and a porosity of 85% are comparable to a 10 ppi CFF. The viscous and inertial permeability were determined before as $k_1 = 1.30 \times 10^{-7}\mathrm{m}^2$ and $k_2 = 2.56 \times 10^{-3}\mathrm{m}$, respectively, for this structure. Considering the kinematic viscosity of liquid steel at 1600 °C, the corresponding superficial velocity is obtained as $u_\mathrm{D} = 61\mathrm{cm/s}$. In order to collect spectral information about the turbulence, the velocity time-series were recorded for selected points over 8 average melt residence times. Subsequently, the spectral density of the fluctuation energy in the longitudinal direction $\overline{u'^2}$ was computed and plotted with respect to the wavenumber κ_1, assuming Taylor's frozen flow hypothesis. The spectra, shown in Fig. 13.9b, indicate a significant heterogeneity of turbulence inside the porous structure: in the pore centre, the fluctuation energy is much higher and also exhibits a wider frequency distribution compared to that at the window, where, however, the average flow velocity is 40% higher. This is also indicated by the turbulence intensity, which reached 34% in the pore centre and 15% in the window. As expected for low Reynolds number turbulence, the inertial subrange, for which the spectrum decays with $\kappa_1^{-5/3}$ is narrow and the transition to the dissipative range occurs early. The variations are also in agreement with model spectra for homogenous isotropic turbulence [32], which were calculated on the basis of the turbulent kinetic energy (TKE) and its dissipation rate, evaluated during the simulation. Figure 13.9c shows the distribution of vorticity in z-direction along a xy-plane, marked in Fig. 13.9a. High values are observed particularly on the sides of the struts, where TKE is produced due to the transient flow separation. The magnified view in Fig. 13.9d shows a small vortex pair at the lower end of the energy spectrum, measuring approximately 50 µm, which is comparable to the size of larger inclusions in metal melts. Since these and the smaller scales are impossible to resolve in practical simulations involving real CFFs, their effects have to be taken care of by appropriate turbulence models. For turbulent flows inside open-cell foams with similar or lower Forchheimer numbers, the Large-Eddy Simulation (LES) was adopted [2]. For this purpose, the spatial resolution, dictated by an accurate representation of the intricate strut network, is sufficient to resolve the bulk of the energy-containing scales, allowing an LES to be performed with no significant additional computational costs. In this respect, two-equation turbulence models were shown to overpredict the TKE near the stagnation point [33]. While reconstructing the unresolved velocity fluctuations for the tracking of inclusions, e.g., using the discrete random walk model (DRWM), this would cause an overestimation of the turbulent dispersion. For further details on the implementation of the LES, the reader is referred to Demuth et al. [2], who demonstrated its application for the simulation of filtration of liquid steel in the turbulent regime. They also analyzed the development and character of the turbulent flow inside the filter and estimated the size of the smallest flow structures.

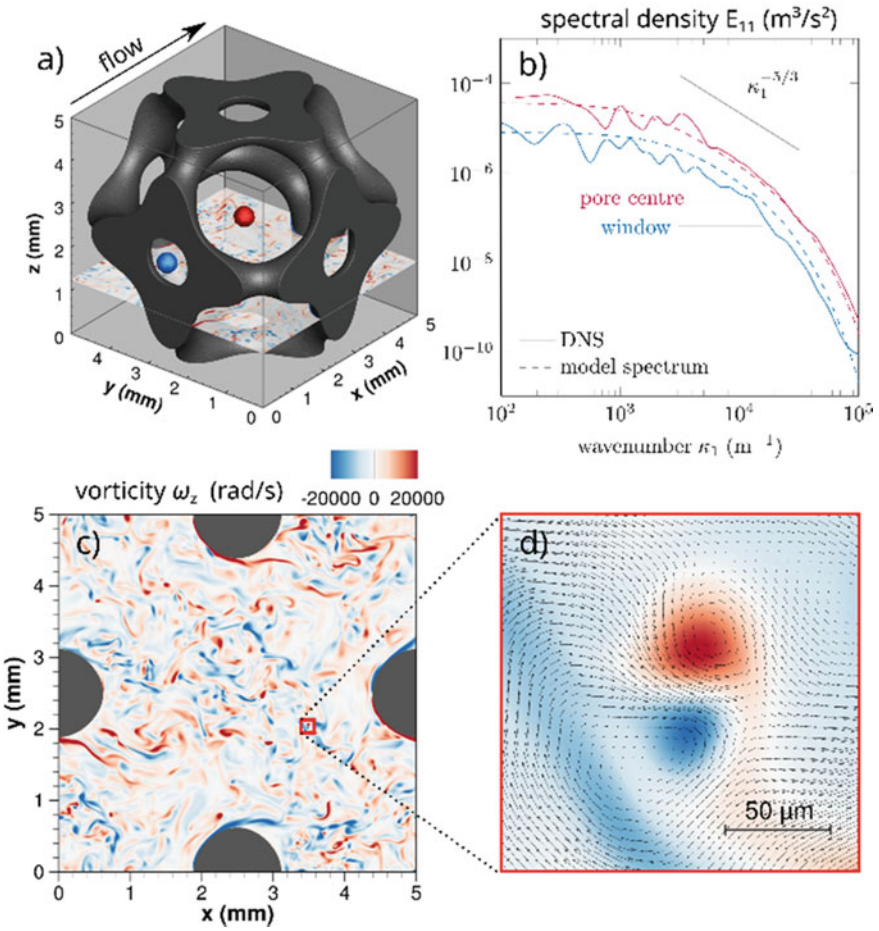

Fig. 13.9 Turbulent flow inside a stack of Kelvin cells mimicking a 10 ppi CFF at $Fo = 64$: **a** simulated periodic unit cell, **b** spectral distribution of longitudinal fluctuation energy for selected locations, **c** distribution of z-vorticity along a plane and **d** magnified section with velocity vectors as seen by a moving observer, showing a small vortex pair

13.5 Sensitivity of the Filtration Process

In the following, the main results of several parametric studies on the sensitivity of the depth filtration process with respect to different process conditions and geometric parameters are presented for the sake of completeness.

As evident from the discussion in Sect. 13.1.3, the filtration efficiency strongly depends on the size of the inclusions. This dependence can be readily observed from Fig. 13.10, which is a result of the simulation of depth filtration of negatively buoyant inclusions inside a stack of 10 ppi filters [5]. While the larger inclusions

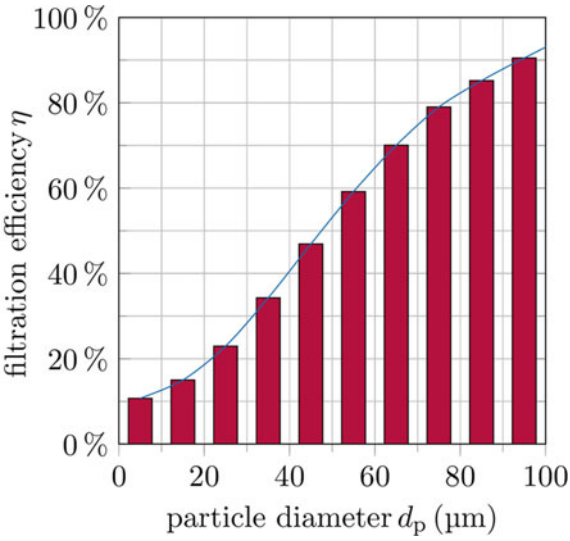

Fig. 13.10 Variation of filtration efficiency for inclusions of different size inside a stack of 10 ppi filters with 54 mm thickness ($\rho_p/\rho_m = 3.96$, $Fo = 2.38$) [5]

are almost certainly filtered, the smaller ones have very low probability of filtration. It has to be mentioned that η should eventually vanish as the size of the inclusions approaches zero, if the Brownian motion is neglected. However, an extremely high spatial resolution or a more accurate boundary treatment would be required in order to capture this behavior. The strong sensitivity of the filtration efficiency with respect to the particle diameter was also observed by Werzner et al. [9, 15], who studied the depth filtration inside CFFs using a 2D idealized filter geometry, consisting of periodic arrays of staggered cylinders, and in 3D computer-generated random open-cell foams.

The bulk velocity of the melt flow affects the individual mechanisms of the filtration process in different ways. For typical melt filtration processes, an increase in the flow rate leads to a higher probability of collisions between the inclusions and the filter struts. This is caused mainly by the fact that, as Forchheimer number increases, the velocity boundary layer becomes thinner, allowing a higher fraction of particles to be intercepted by the struts. This effect was reported by Asad et al. [10], who numerically investigated the depth filtration of non-metallic inclusions with $d_P = 20\mu$m from liquid steel inside Al_2O_3-C foam filters with pore counts of 10 and 20 ppi, neglecting buoyancy effects. As presented in Fig. 13.11a, the filtration coefficient remains constant for very low velocities and starts to increase above approximately 1 mm/s. Figure 13.11b shows the data in dimensionless form, i.e., after normalization of λ using k_2 as filter length scale and plotted with respect to the Forchheimer number. The data seem to approach two distinct asymptotes in the purely viscous and the inertial flow regimes. The macroscopic pressure gradient $p\prime$ was also normalized with respect to k_2, and its variation was found to agree well with the dimensionless form of Eq. (13.6), as visible from Fig. 13.11d. Demuth et al. [2] performed simulations of a similar process at higher Forchheimer numbers using

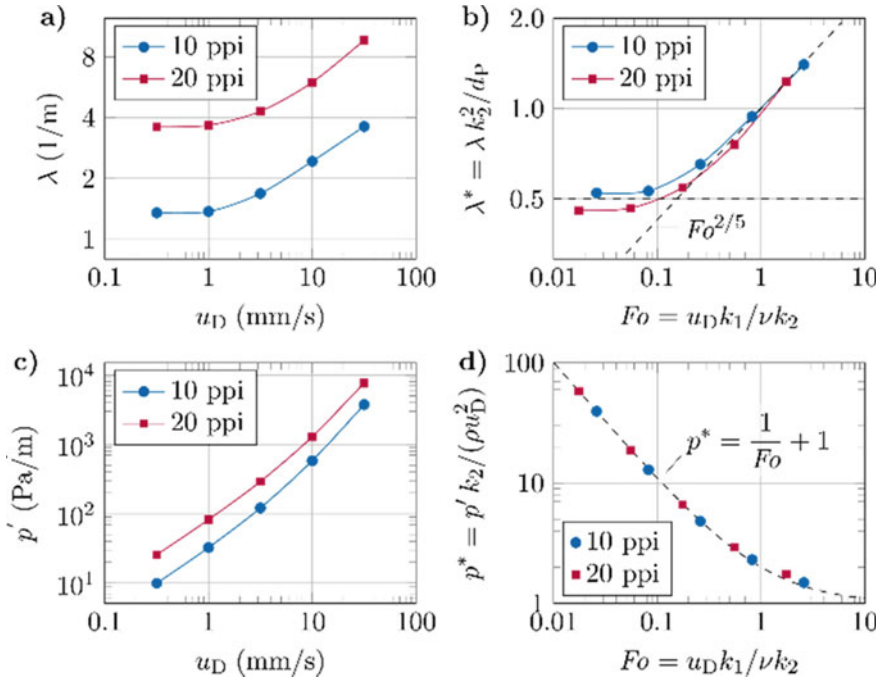

Fig. 13.11 Sensitivity of filtration and pressure gradient with respect to flow velocity during depth filtration of non-metallic inclusions with $d_P = 20\,\mu m$ from liquid steel: variation of **a** filtration coefficient and **c** pressure gradient with superficial velocity and variation of **b** dimensionless filtration coefficient and **d** dimensionless pressure gradient with Forchheimer number [10]

an LES turbulence model. They also observed an increase in the filtration efficiency with the bulk flow velocity, which, however, is less pronounced. This difference may be caused by the pressure gradient term in the equation of motion for the particles that was neglected in the study of Asad et al. [10] and which is expected to reduce the inertial impaction for the positively-buoyant particles. The data from both investigations [2, 10], however show that the gain in filtration efficiency that occurs due to the increase in velocity is obtained at the cost of a lower efficiency in terms of filtration-per-pressure gradient. This is expected since the pressure gradient increases quadratically in the inertial regime. For the sake of completeness it may be mentioned here that the contribution of gravitational settling or buoyant rising to the capture of inclusions decreases with flow velocity and hence can be neglected for most filtration processes [15].

The pore count or pore density is one of the most important geometric parameters for characterizing the filtration performance of open-cell foams. Several studies suggest that the filtration coefficient increases quadratically with the linear pore count, i.e. $\lambda \sim \varphi^{2/3}$. This dependence is confirmed not only by the results obtained from two homogenous structures, presented in Fig. 13.7a, but also can be observed from Fig. 13.11a, while taking into account the actual pore density obtained from

3D image analysis [10]. Demuth et al. also observed a substantial increase in λ with the pore count, which, however, remained sub-quadratic. It is also evident from Fig. 13.11c, that the pressure drop increases with pore count. A dimensional analysis of the Darcy-Forchheimer law clearly shows that the viscous flow resistance scales quadratically with the pore count, while the inertial resistance is only linearly dependent. This is also somewhat visible from Fig. 13.11c, which shows that the ratio in pressure gradient p' for the 10 and 20 ppi CFFs becomes smaller as the inertial regime is approached. The linear relationship in the inertial regime is also confirmed by the difference in pressure drop obtained for the two homogenous structures depicted in Fig. 13.7a. Thus, in the inertial regime, an increase in the pore count is beneficial in terms of the ratio λ/p'.

Owing to the manufacturing process, conventional CFFs exhibit a certain anisotropy, which also affects the characteristics related to metal melt filtration. Werzner et al. [9] observed a maximum variation of 21% in the inertial permeability and up to 10% variation in the filtration coefficient for Al_2O_3 CFFs of 20 and 30 ppi pore count, depending on the flow direction. They suggested to exploit the anisotropy of the filters in order to improve the filtration efficiency or the ratio $\lambda/p\prime$.

The effect of several geometric modifications of a random monodisperse open-cell foam, as presented in Sect. 13.2, on the effective properties related to metal melt filtration was thoroughly investigated from comprehensive parametric studies by Werzner et al. [9] and Lehmann et al. [3]. In these studies, the filtration coefficient was assessed according to the conditions similar to a laboratory-scale trial of aluminum filtration inside a 30 ppi CFF during continuous casting [34] while assuming a constant flow rate. The effect of porosity is presented in Fig. 13.12, where Fig. 13.12d shows that the filtration coefficient increases with decreasing porosity. This could be attributed mainly to the increase in interstitial velocity, which leads to thinner boundary layers and higher velocities near the struts, allowing a larger fraction of inclusions to be intercepted. Towards high porosity, λ seems to approach a finite value, which is also in accordance with the discussion presented in Sect. 13.3.4. An evaluation of the filtration coefficient for the high porosity limit according to Eq. (13.17) yields $\lambda_{\mathrm{lim}} = 4.2$, 8.3 and 16.6m^{-1} for $d_{\mathrm{P}} = 10$, 20 and 40μm, respectively. For this evaluation, the dimensionless specific strut length $l^* = l^+L^2 = 5.39$ of the artificial foam and a reference length $L = 2.94$mm for a 30 ppi filter [9] were considered. Although the theoretical model overpredicts the numerical results, its accuracy may still be considered acceptable in view of its simplicity. As may be observed from Fig. 13.12a, b, the viscous and inertial permeabilities tend to infinity in the high porosity regime, which consequently also applies to the ratio $\lambda/p\prime$. Since l^+ scales quadratically with the linear pore count, an increase in the pore count can be regarded as the most effective way to increase λ in the high porosity regime. The increase in λ for lower porosity is also reflected in the variation of hydraulic tortuosity τ, as shown in Fig. 13.12c. The correlation between both these quantities was observed also by Lehmann et al. [3]. The axial strut shape, i.e., whether the struts have a constant diameter along their axis (solid lines) or are tapered towards the middle (dashed lines) do not significantly affect the behavior.

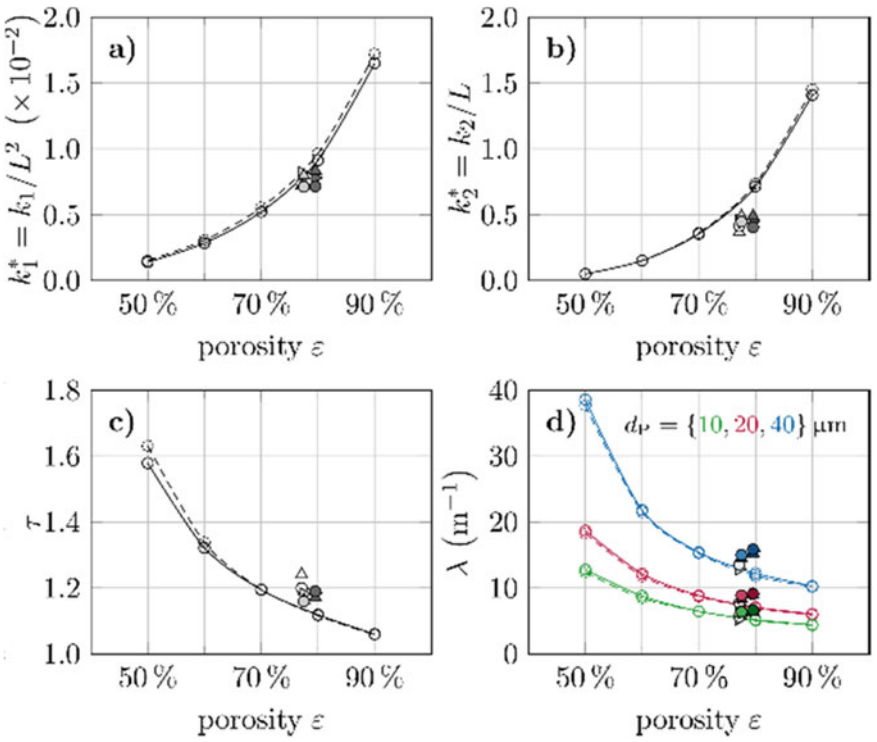

Fig. 13.12 Effect of porosity on effective properties of open-cell foams: **a** dimensionless viscous permeability k_1^*, **b** dimensionless inertial permeability k_2^*, **c** hydraulic tortuosity τ and **d** filtration coefficient λ for Al_2O_3 inclusions of different size employing a scaling, corresponding to a 30 ppi CFF ($L = 2.94$ mm). The solid and dashed lines represent the computer-generated foam with cylindrical and hourglass shaped struts, respectively, whereas the filled symbols are the results for three conventional CFFs, simulated for bulk flow in different directions [9]

With regard to the extended design freedom, enabled by additive manufacturing, Lehmann et al. [3] additionally investigated the effects of closed windows, elliptical strut cross-section and added finger-like struts. Although all modifications eventually lead to an increase in λ, the effect of additional finger-like struts was found to be the most efficient method in terms of filtration per unit pressure drop. This modification could be particularly useful for cases, where an increase in the strut length by increasing the pore count is either difficult or impossible due to the constraints on the manufacturing process.

13.6 Summary and Conclusions

The present investigation contributes to the theoretical characterization, the numerical modeling and the understanding of the depth filtration process, encountered during the removal of non-metallic inclusions from the metal melts using open-cell CFFs. On the basis of theoretical considerations, a modified definition of Stokes number has been proposed, which considers the effect of pressure gradient, allowing to capture the substantial change in the particle dynamics for particle-melt density ratios smaller than unity, which is the case e.g., for steel filtration. Different regimes of fluid flow have been presented in terms of a Reynolds number, which employs the ratio between viscous and inertial permeabilities as the length scale and is believed to indicate the transitions for a broad range of porous media. With regard to effective properties, an extremely simple model for the inertial permeability of CFFs with high porosity has been proposed, which naturally handles the anisotropy and relies only on input parameters that can be easily obtained from CT scan images. Similarly, a simplified model for the prediction of the filtration coefficient in the limit of high porosity has been suggested. Further, recent efforts in the development of simple and detailed methods for the determination of the effective thermal conductivity have been presented. The scale similarity of CFFs between 10 and 30 ppi was shown by normalization of different geometric properties using a length scale derived from the volumetric pore density. As far as the pore-scale simulation of the depth filtration process is concerned, the basic modeling approach was presented and various advanced modeling issues have been demonstrated and discussed. Finally, results of several comprehensive parametric studies on the sensitivity of the filtration process with respect to different process conditions and geometric parameters have been presented and conclusions towards a geometry improvement were drawn.

As evident from the presented results, pore-scale simulations provide good insight into the depth filtration process by giving access to virtually all relevant physical quantities with high temporal and spatial resolution. Nevertheless, for setting up the model itself, a thorough understanding of the involved physical phenomena is required in order to be able to select and parametrize suitable sub-models. The validation of these is often impossible due to the lack of experimental data, which are difficult to obtain for the liquid metal system. Further challenges arise from the computational costs, which usually demand parallel execution on compute clusters and methods for efficient handling of the large amounts of data resulting from such simulations. As the separation step in depth filtration is basically an interface phenomenon, additional care must be taken in order to ensure a sufficient spatial resolution near the filter wall, particularly for the smaller inclusions. High resolution is also required at the melt-gas interface during the infiltration process. While the lattice-Boltzmann method permits the implementation of locally or adaptively refined grids, its simplicity and high parallel efficiency would suffer and a dynamic load balancing may be required. In view of this, other well-established CFD approaches, such as the finite-volume method may be considered equally or more attractive.

The research efforts presented here contribute to the understanding of the filtration process and its sensitivity with respect to geometric characteristics and process conditions, which assists the development of improved filter geometries. It is important to note, however, that besides the removal of unwanted impurities, filters have to also fulfill other tasks that may pose different requirements on geometry. This includes their use for conditioning the turbulent melt flow before it enters the casting mold or the capability for successful priming during the initial stage of filtration under non-ideal conditions, e.g., when a preheating of the filter is not possible. Therefore, these aspects should be addressed in future studies.

Acknowledgements This work was funded by the Deutsche Forschungsgemeinschaft (DFG, German Research Foundation)–Projektnummer 169148856–SFB 920, subproject B02. The authors acknowledge computing time on the compute clusters of the Faculty of Mathematics and Computer Science of Technische Universität Bergakademie Freiberg, operated by the computing center (URZ) and funded by the DFG under grant numbers 397252409 and INST 267 / 159-1 FUGG and would like to thank Oliver Rebentrost and Dieter Simon for the professional support regarding the HPC infrastructure. Further, we would like to thank Jürgen Freitag for his IT support and helpful suggestions and Tommy Flößner for his contributions to the free-surface model.

References

1. C. Demuth, E. Werzner, M.A.A. Mendes, H. Krause, D. Trimis, S. Ray, Adv. Eng. Mater. **19**, 1700238 (2017). https://doi.org/10.1002/adem.201700238
2. C. Demuth, E. Werzner, S. Dudczig, C.G. Aneziris, S. Ray, Adv. Eng. Mater. (2021). https://doi.org/10.1002/adem.202100717
3. H. Lehmann, E. Werzner, A. Malik, M. Abendroth, S. Ray, B. Jung, Adv. Eng. Mater. **24**(2), 2100878 (2021). https://doi.org/10.1002/adem.202100878
4. F. Heuzeroth, J. Fritzsche, E. Werzner, M.A.A. Mendes, S. Ray, D. Trimis, U.A. Peuker, Powder Technol. **283**, 190–198 (2015). https://doi.org/10.1016/j.powtec.2015.05.018
5. D. Hoppach, E. Werzner, C. Demuth, E. Löwer, H. Lehmann, L. Ditscherlein, R. Ditscherlein, U.A. Peuker, S. Ray, Adv. Eng. Mater. **22**, 1900761 (2020). https://doi.org/10.1002/adem.201900761
6. H. Lehmann, E. Werzner, C. Degenkolb, Simulation Series **48**, 32–39 (2016). https://doi.org/10.22360/SpringSim.2016.HPC.043
7. H. Lehmann, E. Werzner, C. Demuth, S. Ray, B. Jung, Efficient visualization of large-scale metal melt flow simulations using lossy in-situ tabular encoding for query-driven analytics, in *21st IEEE International Conference on Computational Science and Engineering* (Bucharest, Romania, 2018)
8. D. Ruth, H. Ma, Transp. Porous Media **7**, 255–264 (1992). https://doi.org/10.1007/BF01063962
9. E. Werzner, M. Abendroth, C. Demuth, C. Settgast, D. Trimis, H. Krause, S. Ray, Adv. Eng. Mater. **19**, 1700240 (2017). https://doi.org/10.1002/adem.201700240
10. A. Asad, E. Werzner, C. Demuth, S. Dudczig, A. Schmidt, S. Ray, C. G. Aneziris, R. Schwarze, Adv. Eng. Mater. **19**, 1700085–n/a, 2017. https://doi.org/10.1002/adem.201700085
11. A. Espinosa-Gayosso, M. Ghisalberti, G.N. Ivey, N.L. Jones, J. Fluid Mech. **783**, 191–210 (2015). https://doi.org/10.1017/jfm.2015.557
12. M. Abendroth, E. Werzner, C. Settgast, S. Ray, Adv. Eng. Mater. **19**, 1700080–n/a (2017). https://doi.org/10.1002/adem.201700080

13. P. Jorge, M.A.A. Mendes, E. Werzner, J.M.C. Pereira, Chem. Eng. Sci. **201**, 397–412 (2019). https://doi.org/10.1016/j.ces.2019.02.010
14. V.M. Patel, M.A.A. Mendes, P. Talukdar, S. Ray, Int. J. Heat Mass Transf. **127**, 843–856 (2018). https://doi.org/10.1016/j.ijheatmasstransfer.2018.07.048
15. E. Werzner, M.A.A. Mendes, S. Ray, D. Trimis, Adv. Eng. Mater. **15**, 1307–1314 (2013). https://doi.org/10.1002/adem.201300465
16. N. Lange, M. Abendroth, E. Werzner, G. Hütter, B. Kiefer, Adv. Eng. Mater. (2021). https://doi.org/10.1002/adem.202100784
17. M.A.A. Mendes, S. Ray, D. Trimis, Int. J. Heat Mass Transf. **66**, 412–422 (2013). https://doi.org/10.1016/j.ijheatmasstransfer.2013.07.032
18. Z. Hashin, S. Shtrikman, J. Appl. Phys. **33**, 3125–3131 (1962). https://doi.org/10.1063/1.1728579
19. R. Wulf, M.A.A. Mendes, V. Skibina, A. Al-Zoubi, D. Trimis, S. Ray, U. Gross, Int. J. Therm. Sci. **86**, 95–103 (2014). https://doi.org/10.1016/j.ijthermalsci.2014.06.030
20. M.A.A. Mendes, S. Ray, D. Trimis, Int. J. Therm. Sci. **79**, 260–265 (2014). https://doi.org/10.1016/j.ijthermalsci.2014.01.009
21. M.A.A. Mendes, S. Ray, D. Trimis, Int. J. Heat Mass Transf. **75**, 224–230 (2014). https://doi.org/10.1016/j.ijheatmasstransfer.2014.02.076
22. P. Talukdar, M.A.A. Mendes, R.K. Parida, D. Trimis, S. Ray, Int. J. Therm. Sci. **72**, 102–114 (2013). https://doi.org/10.1016/j.ijthermalsci.2013.04.027
23. M.A.A. Mendes, P. Talukdar, S. Ray, D. Trimis, Int. J. Heat Mass Transf. **68**, 612–624 (2014). https://doi.org/10.1016/j.ijheatmasstransfer.2013.09.071
24. L.-M. Heisig, K. Markuske, E. Werzner, R. Wulf, T.M. Fieback, Adv. Eng. Mater. (2021). https://doi.org/10.1002/adem.202100723
25. M.A.A. Mendes, V. Skibina, P. Talukdar, R. Wulf, U. Gross, D. Trimis, S. Ray, Int. J. Heat Mass Transf. **78**, 112–120 (2014). https://doi.org/10.1016/j.ijheatmasstransfer.2014.05.058
26. P. Götze, M.A.A. Mendes, A. Asad, H. Jorschick, E. Werzner, R. Wulf, D. Trimis, U. Groß, S. Ray, Spec. Top. Rev. Porous Media **6**, 1–10 (2015). https://doi.org/10.1615/SpecialTopicsRevPorousMedia.v6.i1.10
27. M.A.A. Mendes, P. Götze, P. Talukdar, E. Werzner, C. Demuth, P. Rößger, R. Wulf, U. Groß, D. Trimis, S. Ray, Int. J. Heat Mass Transf. **102**, 396–406 (2016). https://doi.org/10.1016/j.ijheatmasstransfer.2016.06.022
28. A. Duda, Z. Koza, M. Matyka, Phys. Rev. E **84**(3), 036319 (2011). https://doi.org/10.1103/PhysRevE.84.036319
29. E. Werzner, M. Mendes, S. Ray, D. Trimis, Numerical modeling of long-term depth filtration of metal melts inside open-cell ceramic foams, in *Proceedings CellMAT* (Dresden, Germany, 2014)
30. T. Flößner, Numerical modeling of the infiltration of open-cell ceramic foams during metal melt filtration using the lattice-Boltzmann method, Master thesis, Institute of Thermal Engineering, Technische Universität Bergakademie Freiberg, 2017
31. C. Voigt, L. Ditscherlein, E. Werzner, T. Zienert, R. Nowak, U. Peuker, N. Sobczak, C.G. Aneziris, Mater. Des. **150**, 75–85 (2018). https://doi.org/10.1016/j.matdes.2018.04.026
32. S.B. Pope, *Turbulent flows* (Cambridge University Press, Cambridge, UK, 2000)
33. F. Kuwahara, T. Yamane, A. Nakayama, Int. Commun. Heat Mass Transfer **33**, 411–418 (2006). https://doi.org/10.1016/j.icheatmasstransfer.2005.12.011
34. P. L. Brun, F. Taina, C. Voigt, E. Jäckel, C. Aneziris, Assessment of Active Filters for High Quality Aluminium Cast Products, in *Light Metals* (Hoboken, 2016)